Cancer-associated metabolic alterations facilitated by astrocyte glycogenolysis mediate neuropathic pain chronicity

Junseo Park[1,2], Kwanghwan Kim[3], Hyewon Jun[3], Sung Joong Lee[4 *]

[1]Department of Environmental Materials Science, College of Agriculture and Life Sciences, Seoul National University, Seoul, Republic of Korea.
[2]Department of Chemistry, College of Natural Sciences, Seoul National University, Seoul, Republic of Korea.
[3]Interdisciplinary Program in Neuroscience, College of Natural Science, Seoul National University, Seoul, Republic of Korea
[4]Department of Physiology and Neuroscience, Dental Research Institute, Seoul National University School of Dentistry, Seoul, Republic of Korea.

*Corresponding author

Abstract

Metabolic signaling in astrocytes has been implicated in a range of neurophysiological disorders[1,2]. Likewise, pain chronification, which is defined as the transition from an acute pain state to a persistent one in response to repeated or intense nociceptive stimuli, involves crucial contributions from astrocytes[3,4]. Although lactate transport by anterior cingulate cortex (ACC) astrocytes has been shown to influence pain chronification, the specific metabolic pathways and upstream signaling events remain poorly understood[4,5]. In this study, we identified glycogenolysis in ACC astrocytes as a central signaling mechanism controlling pain chronification. Inhibition of glycogenolysis suppressed pain-related behaviors and normalized neuronal hyperactivity. To extend the effects of glycogenolysis to broader metabolic dynamics, we conducted integrated transcriptomic and metabolomic analyses as chronic pain progressed. Interestingly, those analyses revealed that chronic pain was accompanied by a shift toward cancer-associated metabolic programs in the ACC, and that shift was driven by astrocytic glycogenolysis. Taken together, our findings demonstrate that pain chronification is mediated by astrocytic glycogenolysis, which induces a cancer-associated metabolic pathway. Therefore, alterations in astrocytic glycogen metabolism could be key signals for cancer-associated metabolic reprogramming. These findings offer novel insights into astrocyte-driven oncogenic metabolic regulation in neuropathic pathology.

Main

Neuropathic pain is a chronic pathological pain state arising from injury or dysfunction of the nervous system[3,6]. Repeated or intense nociceptive stimuli can drive the transition from acute to persistent pain[6,7]. This chronification is mediated by diverse adaptations within the central nervous system, including alterations in neuronal excitability and synaptic plasticity[3,7].

Glycogen metabolism is a well-established mechanism underlying neuronal excitability and associated behaviors[8,9]. Notably, glycogen metabolism is primarily confined to astrocytes in the central nervous system, where its metabolites support and regulate neuronal excitability, particularly in response to traumatic stimuli[5,10,11]. By extension, dynamic shifts in astrocytic glycogen turnover might similarly contribute to the development of chronic pain. Indeed, modulation of glycogen dynamics in spinal cord astrocytes prevents the establishment of persistent pain, but the role of astrocytic glycogen metabolism in supraspinal pain circuits remains unexplored[5,10]. In the anterior cingulate cortex (ACC), inhibiting the transport of astrocyte-derived lactate—a product of glycogen metabolism—attenuated both pain chronification and neuronal hyperactivity[4,12,13]. However, how peripheral traumatic injury alters the dynamics of brain glycogen metabolism, thereby contributing to pain chronification, remains elusive.

Unlike non-transformed cells, cancer cells must simultaneously fulfill demands for ATP generation, biosynthetic precursor supply, and reducing power to sustain their unchecked proliferation and growth[14]. To meet those requirements, tumor cells enact extensive metabolic reprogramming by remodeling pathways for glucose, amino acid, and lipid utilization; we define that reprogramming as cancer-associated metabolism[14,15]. In hypoxic conditions, oncogenic transcription factors such as HIF-1α and c-Myc enhance this adaptive flexibility by upregulating the expression of key metabolic enzymes[15].

A hallmark of cancer-associated metabolism is the Warburg effect, by which cancer cells convert most imported glucose into lactate—even in the presence of ample oxygen[14,16]. This aerobic glycolysis enables rapid ATP production at short timescales and generates abundant intermediate metabolites to serve as building blocks for nucleotide, amino acid, and lipid synthesis[16]. Moreover, lactate accumulation acidifies the tumor microenvironment, thereby impairing effector immune cell function and fostering a pro-inflammatory milieu that can facilitate tumor progression[16].

Cancer cells also exploit glutamine-driven glutaminolysis to replenish tricarboxylic acid (TCA) cycle intermediates via anaplerosis and thus sustain continuous biosynthetic output[14,15,17]. By channeling glutamine into the TCA cycle, tumor cells not only maintain their energy flux but also divert TCA intermediates into the synthesis of proteins, lipids, and antioxidants such as glutathione[17]. Together, these complementary pathways underpin the metabolic flexibility essential for tumor growth, survival, and metastatic potential[17].

In this study, we demonstrate that astrocyte glycogen metabolism in the ACC is reprogrammed during neuropathic pain chronification in mice. A pharmacological blockade of glycogenolysis in the ACC rescued glycogen metabolism, neuronal hyperactivation, and pain chronification. Integrated transcriptomic and metabolomic profiling revealed the upregulation of cancer-associated metabolic pathways—akin to the Warburg effect—during the transition from acute to chronic pain, and that upregulation was reversed by glycogenolysis inhibition. These findings uncover a novel astrocyte-centric metabolic mechanism driving chronic pain.

To investigate glycogen metabolic dynamics in the brain during pain chronification, we harvested the ACC, a supraspinal hub for chronic pain processing[18], from mice 1, 3, 5, and 7 days after spinal nerve transection (SNT). We induced neuropathic pain in mice by transecting the L5 spinal nerve[19,20,21], and we followed that by performing a colorimetric glycogen assay (Fig. 1a). We confirmed that the SNT mice developed chronic mechanical allodynia (Fig. 1b). Correspondingly, in the ACC contralateral to the injured nerve (contraACC), glycogen accumulated from day 1 to day 3 post-injury and then declined to baseline by day 7 (Fig. 1c).

Glycogen is metabolized to lactate, a proposed chronic pain mediator[4], through

glycogenolysis[10]. To investigate whether brain glycogenolysis contributes to pain chronification, we targeted the brain-specific glycogen phosphorylase isoform B (PYGB)[8,9]. We selected two chemically distinct PYGB inhibitors[22,23,24]—GPI-1 (5-chloro-N-[(1S,2R)-2-hydroxy-3-(methoxymethylamino)-3-oxo-1-(phenylmethyl)propyl]-1H-indole-2-carboxamide) and GPI-2 (1-[3-(3-[2-chloro-4,5-difluorobenzoyl]ureido)-4-methoxyphenyl]-3-methylurea)—and confirmed their appropriate binding interactions with PYGB using an *in silico* docking analysis[25,26] (Extended Data Fig. 1a–d).

To test whether PYGB inhibition influences pain chronification and glycogenolytic products, we stereotaxically injected GPI-1 or GPI-2 directly into the contraACC of SNT mice and then conducted the von Frey test and nuclear magnetic resonance (NMR) spectroscopy (Fig. 1d). In both the GPI-1 and GPI-2 treated groups, chronic mechanical allodynia was rescued across the testing days (Fig. 1e), although they exhibited acute mechanical sensitivity comparable to the SNT control group on day 1 (Fig. 1e). Seven days after SNT, we harvested the contraACC and performed NMR to quantify the glycogenolytic product glucose-1-phosphate (G1P). We found that G1P was significantly increased in the SNT control mice, and that increase was reversed by both PYGB inhibitors (Fig. 1f).

We further tested neuronal activation levels in the contraACC by measuring immunohistochemical cell activation markers[4]: c-Fos, pCREB, and p-p38-MAPK. The number of c-Fos–positive neurons was elevated in SNT control mice relative to the sham-operation controls, and it was significantly decreased following GPI-1 or GPI-2 treatment (Fig. 1g, h). Likewise, although both pCREB- and p-p38–positive neurons in the contraACC were enriched in the SNT mice, treatment with either GPI normalized their expression to sham levels (Extended Data Fig. 2a–d).

Given that ACC output to the nucleus accumbens (NAc) and ventral tegmental area (VTA) contributes to affective behaviors during chronic pain[27,28], we examined c-Fos expression in those regions. In both the NAc and VTA contralateral to the injured nerve, SNT robustly induced neuronal activation, which was reversed by treatment with either GPI in the contraACC (Extended Data Fig. 3a–d). Together, these data demonstrate that blocking glycogenolysis in the ACC following SNT injury attenuates both local and circuit-wide neuronal hyperactivity.

In the central nervous system, glycogen metabolism is largely confined to astrocytes[8,9,10]. To further support and confirm that assertion, we analyzed publicly available single-cell RNA sequencing data[29]. We found that key glycogen metabolic enzyme transcripts[5,8,9,10]—glycogen synthase 1 (*Gys1*), *Pygb*, phosphorylase kinase regulatory subunit alpha 2 (*Phka2*) and protein phosphatase 1 regulatory subunit 3C (*Ppp1r3c*)—are highly enriched in astrocyte clusters, with minimal expression in neurons or other glia (Fig. 2a, b).

We next asked whether the gene expression of glycogen metabolic enzymes in astrocytes changes over time in parallel with glycogen dynamics during pain chronification (Fig. 1c). To achieve astrocyte-specific mRNA profiling within defined time windows after SNT, we isolated translating mRNAs from the ACCs of GFAP^{Cre}::RiboTag mice[30,31] and quantified *Gys1*, *Pygb*, *Phka2*, and *Ppp1r3c* (Fig. 2c, Extended Data Fig. 4a–c). All four enzyme genes exhibited distinct temporal profiles during the transition from acute to chronic pain. Notably, the expression of *Ppp1r3c*—an activator of glycogenolysis—was highest when glycogen levels peaked, whereas *Pygb* expression reached its maximum on day 7 post-injury (Fig. 2d). These data indicate that the astrocytic glycogen machinery undergoes reprogramming during neuropathic pain chronification.

To directly assess the contribution of astrocytes to pain chronification, we selectively

ablated ACC astrocytes by overexpressing caspase-3[32,33] and then performed SNT surgery (Fig. 2e). We first confirmed astrocyte depletion in the contraACC by staining the immunohistochemical astrocyte marker S100β (Fig. 2f). The ablation of astrocytes did not alter acute pain thresholds, but it elevated chronic pain thresholds post-SNT to levels similar to those of mice in the sham group (Fig. 2g). We then quantified c-Fos–positive neurons in the contraACC. Consistent with our PYGB inhibition results (Fig. 1g, h), astrocyte-ablated mice showed a significant reduction in c-Fos–expressing neurons, compared with the SNT controls (Fig. 2h–j). These findings demonstrate that ACC astrocytes are critical for the transition from acute to chronic pain, indicating the functional role of astrocyte glycogenolysis in pain chronification.

Glycogen breakdown is linked to the Warburg effect[9,16]. Accordingly, we quantified the translation of mRNA associated with the Warburg effect using GFAP^{Cre}::RiboTag mice (Fig. 3a, Extended Data Fig. 4a–c). Hypoxia-inducible factor 1-a (*Hif-1a*), lactate dehydrogenase a (*Ldha*) and b (*Ldhb*), and monocarboxylate transporter 4 (*Mct4*) exhibited dynamic changes during pain chronification[14,15,16]. Notably, *Hif-1a* exhibited a prominent peak, and *Ldha* and *Mct4* showed pronounced upregulation at the chronic pain time point (Fig. 3b).

In a parallel analysis, we examined transcriptomic profiles from the contraACC in a chronic constriction injury (CCI) model[34], which recapitulates features of SNT-induced neuropathic pain (Extended Data Fig. 5a). Seven days post-CCI, contraACC expression data were normalized against sham controls, and a gene set enrichment analysis (GSEA) was performed for each pathway of interest[35] (Extended Data Fig. 4b–f). The GSEA plots indicate significant upregulation of the Warburg effect and glutamate metabolism pathways in chronic pain conditions (Extended Data Fig. 5b, c). In contrast, aerobic glycolysis—as opposed to the Warburg phenotype—and the TCA cycle and oxidative phosphorylation (OXPHOS) pathways were all downregulated (Extended Data Fig. 5d–f). These results confirm that, at the transcriptomic level, cancer-associated metabolic programs such as the Warburg effect and glutamate metabolism are selectively enacted during the chronic state of neuropathic pain.

Because gene expression provides only indirect information about downstream metabolites[36,37,38], we directly assessed metabolite fluxes by performing GC-MS–based metabolomics on ACC tissue collected at defined intervals following SNT (Fig. 3c). Individual metabolites displayed dynamic, time-dependent profiles. Notably, several central carbon intermediates and amino acids progressively accumulated as pain transitioned from the acute to chronic state (Fig. 3d). To systematically evaluate these metabolic changes, we performed pathway enrichment analyses[37]. During the course of pain chronification, the Warburg effect and glutamate metabolism emerged as the most strongly enriched pathways (Fig. 3e–f). Moreover, multiple cancer-associated metabolic pathways were upregulated during the transition from acute to chronic pain (Fig. 3g).

To test how blocking astrocytic glycogenolysis would reshape metabolic networks in the ACC, we stereotaxically injected GPI-1 or GPI-2 into the contraACC of SNT mice and performed 1H-NMR metabolomics on day 7 post-injury[39,40] (Fig. 4a). The metabolite concentrations determined by NMR were compared across groups (Fig. 4b–k, Extended Data. 6a–d).

In the SNT controls, lactate was significantly increased, relative to the sham group, but both GPI-1 and GPI-2 treatment restored the lactate level to baseline (Fig. 4b). We next examined key metabolites of the TCA cycle and glutamate metabolism. The SNT animals exhibited reduced succinate and increased pyruvate and malate, compared with the sham group;

PYGB inhibition reversed the latter two elevations, lowering pyruvate and malate toward sham values (Fig. 4c–e). Although glutamine and GABA showed no significant changes across groups, glutamate increased markedly after SNT, and it was significantly attenuated by GPI-1 and GPI-2 (Fig. 4f–h).

Focusing on the cancer-associated pathways highlighted by our GC-MS screen (Fig. 3), we performed pathway-level enrichment analyses of the NMR data for the Warburg effect and glutamate metabolism[37]. Both the enrichment p-value and expectation value for these pathways were substantially lower in the PYGB-inhibited groups than the SNT controls (Fig. 4m–n). Furthermore, although SNT drove broad activation of multiple oncometabolic pathways, PYGB blockade substantially reduced both the impact scores and statistical significance of those pathways (Extended Data. 6e–g).

Collectively, these results demonstrate that astrocytic glycogenolysis in the ACC critically governs cancer-associated metabolic reprogramming—modulating lactate production, TCA cycle flux, and glutamate turnover—and that PYGB inhibition restores these maladaptive metabolic circuits and prevents pain chronification.

In summary, this study reveals that peripheral nerve injury modulates glycogen metabolism in brain astrocytes, causing neuropathic pain to progress to a chronic state. We found that glycogenolysis in ACC astrocytes is the key metabolic regulation associated with neuropathic pain chronification. Within the ACC, glycogen metabolic dynamics emerge during the chronification of neuropathic pain, and astrocyte-derived glycogenolysis promotes pain chronification by enhancing neuronal excitability. Moreover, the modulation of ACC astrocyte glycogenolysis controls cancer-associated metabolic changes—particularly the Warburg effect and glutamate metabolism—and thereby governs the chronification process. This finding represents the discovery of a novel glycogen-dependent astrocytic signaling mechanism that drives pain chronicity and provides the first elucidation of astrocyte-mediated pain chronification from the perspective of metabolic pathway dynamics.

Our transcription-metabolome analysis demonstrated that nerve injury–promoted astrocytic glycogen metabolism was closely associated with the Warburg effect and other oncogenic metabolic alterations. This suggests that cancer-inducing molecular dynamics changes could have a distinctive neurophysiological effect in the brain that regulates pain and its related affective behaviors. Astrocyte metabolism has traditionally been viewed primarily as a means of regulating neuronal energy supply and neurotransmitter provision[41,42]. However, based on the alterations in cancer-associated metabolic programs revealed in this study, we propose that astrocytes can influence pathological processes not only by supplying metabolites to neurons but also through intrinsic shifts in their own metabolic flux. In particular, the activation of cancer-associated metabolism implies a range of functional consequences. In classical cancer cells, oncogenic metabolic alteration not only activates and supports metabolic pathways but also plays critical roles in immune evasion and the regulation of inflammatory responses. By analogy, such metabolic alterations in astrocytes could serve as a central mechanism for modulating diverse functions—including the activation of inflammatory pathways and the control of immune responses—via oncogenic-like metabolic shifts. We anticipate that such alterations in astrocytic metabolic dynamics will yield novel insights into the mechanisms underlying neurophysiological disorders and also highlight important targets for the development of new therapeutic strategies.

Methods

Animals

All animal experiments were approved by the Institutional Animal Care and Use Committee of Seoul National University. GFAP-Cre and Rpl22$^{HA/HA}$ (RiboTag) mice were obtained from Jackson Laboratory (GFAP-Cre: B6.Cg-Tg.Gfap-cre.77.6Mvs/2J, Rpl22$^{HA/HA}$: B6.129-Rpl22tm1.1Psam/J). We generated astrocyte-specific RiboTag mice by crossing floxed RiboTag mice with GFAP-Cre transgenic mice. The genotypes of the offspring were determined by PCR with the following primers:
GFAPcre-Fw: TCC ATA AAG GCC CTG ACA TC; *GFAPcre*-Rv: TGC GAA CCT CAT CAC TCG T; *RiboTag*-Fw: GGG AGG CTT GCT GGA TAT G; *RiboTag*-Rv: TTT CCA GAC ACA GGC TAA GTA CAC
Except for the RiboTag experiments, all mice used were C57BL/6. Male and female C57BL/6 mice (8–12 weeks of age) were purchased from DooYeol Biotech (Seoul, Korea). All animals were acclimatized to standard conditions with a 12-hr light/dark cycle in a specific pathogen-free environment and given access to chow and water *ad libitum*. All protocols were performed in accordance with guidelines from the International Association for the Study of Pain.

Neuropathic pain mouse model

To generate a persistent pain model, right L5 SNT was performed as previously described[43]. Briefly, animals were anesthetized with isoflurane in an O_2 carrier (induction 2% and maintenance 1.5%), and a small incision was made to expose the L4 and L5 spinal nerves. The L5 spinal nerve was then transected.

Pain behavior test (von-Frey test)

Mechanical sensitivity of the right hind paw was assessed using a calibrated series of von Frey hairs (0.02–6 g, Stoelting, Wood Dale, IL, USA) and following the up-down method[44]. Tests were performed after at least three habituations at 24-hr intervals. Assessments were made 1 day before surgery for baseline, and 1, 3, 5, and 7 days after SNT. Rapid paw withdrawal, licking, and flinching were interpreted as pain responses. All behavioral tests were performed blinded to condition.

Stereotaxic injection

For stereotaxic drug injection, each C57BL/6 mouse received a unilateral injection of 1 μl of GPI-1 at 500 nM (CP-316819, CAS 186392-43-8; TOCRIS, Minneapolis, MN, USA) or 1 μl of GPI-2 at 300 nM (361515-1MG, CAS 648926-15-2; Sigma-Aldrich, St. Louis, MO, USA) in the ACC using the following coordinates: AP, −1.0 mm; ML, 0.4 mm; DV, −1.5 mm from the bregma. SNT surgery was performed 1 h after the drug injections.
For stereotaxic virus injection, each C57BL/6 mouse received a unilateral injection of 1 μl of pAAV-flex-a-taCasp3-TEVp, AAV-GFAP-Cre-WPRE-hGH, or AAV5-gfaABC1D-tdTomato (~1×10^{13} gene copies (GC)/ml) in the ACC using the following coordinates: AP, −0.9 mm; ML, 0.4 mm; DV, −1.5 mm from the bregma. SNT surgery was performed 4 weeks after the virus injections. The injection syringe (Hamilton, Reno, NV, USA) delivered GPI or AAV at a constant volume of 0.1 μl min^{-1} using a syringe pump (Stoelting, Wood Dale, IL, USA).

Immunohistochemistry (IHC)

Mice were transcardially perfused with ice-cold 0.1 M phosphate-buffered saline (PBS; pH 7.4) until all blood was removed, followed by perfusion with ice-cold 4% paraformaldehyde in

0.1 M PBS. Whole brains were post-fixed in 4% paraformaldehyde in 0.1 M PBS overnight at 4°C and cryoprotected with 30% sucrose for 3 days. Coronal 60-μm-thick sections were incubated in cryoprotectant at −20°C until immunohistochemical staining was performed. The sections were incubated for 1 h at room temperature in a blocking solution containing 5% normal goat serum (Jackson ImmunoResearch, Bar Harbor, ME, USA), 2% BSA (Sigma-Aldrich), and 0.1% Triton X-100 (Sigma-Aldrich).
Subsequently, the sections were incubated in the blocking solution with mouse anti-NeuN (MAB377B, 1:1000; Millipore, Billerica, MA, USA), rabbit anti-S100β (ab52642, 1:500; Abcam, Cambridge, MA, USA), mouse anti-phospho-CREB (#9198 87G3, 1:1000; Cell Signaling Technology, Danvers, MA, USA) rabbit anti-p-p38 MAPK (# 9211S, 1:1000; Cell Signaling Technology), or rabbit anti-c-Fos (#2250 9F6, 1:1000; Cell Signaling Technology) antibodies overnight at 4°C. After being washed with 0.1 M PBS containing 0.1% Triton X-100, the sections were incubated in the blocking solution for 1 h with FITC-, Cy3- or Cy5-conjugated secondary antibodies (1:200, Jackson ImmunoResearch) at room temperature, washed three times, and then mounted on gelatin-coated glass slides using Vectashield (Vector Laboratories, Inc., Burlingame, CA, USA). Fluorescent images of the mounted sections were obtained using a confocal microscope (LSM800; Carl Zeiss, Jena, Germany).

Glycogen assay

Sample preparation
For brain sections, the animals were killed under isoflurane, and the brain was quickly released from the skull and immediately frozen with dry ice. ACC sections were collected based on measurements from the Allen brain atlas, and the samples were snap-frozen and kept at −80°C until further processing.

Glycogen colorimetric assay
Tissue samples were homogenized on ice in 200 μL of ddH_2O using a Dounce homogenizer with 10–15 passes. Homogenates were boiled for 10 min to inactivate enzymes and subsequently centrifuged at 18,000 × g for 10 min at 4°C to remove insoluble material. The resulting supernatant was collected and used for the glycogen analysis. To perform the assay, 2–50 μL of the tissue supernatant was added to a 96-well plate, and the volume was adjusted to 50 μL per well with glycogen hydrolysis buffer provided in the glycogen colorimetric/fluorometric assay kit (ab65620, Abcam). For glycogen detection, 2 μL of hydrolysis enzyme mix was added to the wells designated for glycogen hydrolysis, and the background control wells received no enzyme. The samples were incubated at room temperature for 30 min to allow the hydrolysis of glycogen to glucose.
Following hydrolysis, 50 μL of a reaction mix containing 46 μL of development buffer, 2 μL of development enzyme mix, and 2 μL of OxiRed probe was added to all wells. The plates were then incubated in the dark at room temperature for 30 min. Absorbance was measured at 570 nm using a microplate reader to quantify the glycogen content. A standard curve was generated using glycogen standards (0–2 μg/well) prepared according to the manufacturer's instructions to determine the sample glycogen concentrations. Background absorbance from control wells was subtracted from the sample wells to account for any non-glycogen-derived signal. The glycogen concentration in each sample was normalized to the initial sample volume and adjusted based on dilution factors.

$$OD_{corrected} = OD_{sample} - OD_{background}$$

OD sample: Measured OD value for the sample well.
OD background: Measured OD value for the sample background control well (except hydrolysis mix – measured-only background glucose constant).

$$Glycogen\ constant\ (\mu g/well) = \frac{OD_{corrected} - b}{m}$$

m: Slope of the standard curve (glycogen constant).
b: Intercept of the standard curve.
OD corrected: Corrected OD value for the sample well.

Western blotting

For Western blotting, ACC tissues were homogenized in ice-cold RIPA buffer (50 mM Tris-HCl pH 7.5, 150 mM NaCl, 1% NP-40, 0.5% sodium deoxycholate, 0.1% SDS) supplemented with 1 mM PMSF and phosphatase inhibitor cocktail (Sigma-Aldrich, P5726). The homogenates were incubated on ice for 30 min and centrifuged at 13,000 rpm for 15 min at 4°C, and then the supernatants were collected. Protein concentration was measured using a BCA assay (Pierce, 23225), and 20 µg of each sample was mixed with 5× SDS sample buffer, boiled for 5 min at 95°C, and then resolved on 10% SDS-PAGE. Proteins were transferred to nitrocellulose membranes (LC2001; Invitrogen, Carlsbad, CA, USA) at 100 V for 1 h, blocked in 5% milk/TBST for 1 h, and probed overnight at 4°C with mouse anti-HA (ab9110, 1:2000; Abcam) and mouse anti-β-actin (A2228, 1:5000; Sigma-Aldrich) in 2.5% milk/TBST. After three TBST washes, the membranes were incubated with HRP-conjugated goat anti-mouse IgG (1:3000 in 2.5% milk/TBST) for 1 h at room temperature. Blots were developed with SuperSignal™ West Pico PLUS (Thermo Fisher, Waltham, MA, USA) and imaged on a Fusion FX6.0 system; band intensities were quantified in ImageJ and normalized to β-actin.

qPCR

The real-time RT-PCR (qPCR) experiments were performed using a StepOnePlus real-time PCR system (Applied Biosystems, Foster City, CA, USA) following the $2^{-\Delta\Delta Ct}$ method. Total RNA from contraACC tissue was extracted using TRIzol (Invitrogen) and reverse transcribed using TOPscript RT DryMIX (Enzynomics, Cat # RT200, Daejeon, Korea). All the ΔCt values were normalized to the corresponding GAPDH values, and they are represented as fold change induction.

qPCR primers used:

Ppp1r3c-Fw: GGT GAC TCA TCT TTC TGC CAC A; *Ppp1r3c*-Rv: CAA GAC AAA ATT AGG CAC GAG A; *Gys1*-Fw: ATC TAC ACT GTG CTG CAG ACG; *Gys1*-Rv: CCC TTG CTG TTC ATG GAA TCC; *Phka2*-Fw: TGG ATG CCA CCT CTC TCT TC; *Phka2*-Rv: TAT CTC CAC GCT CCC ACA TC; *Pygb*-Fw: CAG CAG CAT TAC TAT GAG CGG; *Pygb*-Rv: CCA AGT CCA ACC CCA ACT GA; *Hif-1a*-Fw: GAT CCT TGA TGC TTG CTG GG; *Hif-1a*-Rv: CTG TCC CCA ATG TCC AGA GT; *Ldha*-Fw: AAA GAG GAC TAA GGG GTG GC; *Ldha*-Rv: CTG CAG GAA ACA ACC ACT CC; *Ldhb*-Fw: AAA GGC TAC ACC AAC TGG GC; *Ldhb*-Rv: GCC GTA CAT TCC CTT CAC CA; *Mct4*-Fw: CAT TCC CAG GGA CGC AAA GAG; *Mct4*-Rv: GAC ACG GCT TGG ATC TCC TC

RNA-seq data analysis

Raw RNA-seq data were processed in Python to analyze relative gene expression between the experimental and control groups. Raw counts were compared against the sham group and

normalized for library size using DESeq2's size-factor adjustment. A negative-binomial model was then fitted to calculate the $\log_2$ fold change and associated p-value for each gene. Genes were ranked in descending order by their $\log_2$FC/standard error, and a GSEA was performed against the Hallmark and Gene Ontology gene sets. Normalized enrichment scores and false discovery rates were computed, and enrichment plots were generated in GraphPad Prism. For each analysis, we selected gene sets corresponding to specific metabolic pathways to assess their degree of enrichment.

GC-MS

Tissue samples for the GC-MS analysis were prepared from the ACC using the same dissection and freezing protocol as for the glycogen assay. For each contraACC specimen, 400 µL of tissue supernatant was collected and subjected to GC-MS. Derivatization was performed using trimethylsilylation, and 1 µL of each derivatized sample was injected into a Thermo Scientific ISQ LT GC-MS system (Thermo Scientific, Waltham, MA, USA). Chromatographic separation and mass detection were carried out in standard operating conditions. Raw data were processed in Thermo Xcalibur Quan Browser: metabolites were identified by matching each chromatographic peak to reference spectra, and peak areas were integrated against baseline to obtain relative signal intensities. All metabolite abundances were then normalized to the sham controls and expressed as fold changes for downstream analysis.

NMR

Tissue for the NMR analyses of the ACC was prepared using the same dissection and freezing protocol as for the glycogen assay. For each contraACC sample, 500 µL of the tissue supernatant was collected and analyzed by NMR. Spectra were acquired on a Bruker AVANCE III HD 600 MHz high-resolution NMR spectrometer (Bruker BioSpin, Rheinstetten, Germany). Individual resonances were assigned using Chenomx NMR Suite Profiler, and metabolite concentrations were determined by integrating each peak relative to the subtraction baseline.

Metabolomics analysis

Absolute and relative metabolite concentrations obtained by GC-MS and NMR—including fold-change values normalized to the sham controls—were subjected to a comprehensive metabolomics analysis. For each metabolite, both the absolute abundance and fold-change relative to the sham and saline + SNT groups were calculated, and statistical significance was assessed. To identify enriched metabolic pathways within each experimental group, we performed both an over-representation analysis and a quantitative enrichment analysis. All pathway enrichment analyses were conducted using MetaboAnalyst v6.0. (http://www.metaboanalyst.ca).

In-silico analysis

Ligand coordinates were generated in silico from the canonical SMILES string. Hydrogens were added, and the geometry was energy-minimised to convergence; the lowest-energy conformer was exported in PDB format. Protein coordinates (PDB) were parsed with a structural biology toolkit to extract atom- and residue-level information. Ligand residues were recognised by residue name, and neighbouring amino acids within a predefined distance cutoff were designated as pocket residues.

These pocket residues were recorded for subsequent validation and docking calculations to characterise protein–ligand interactions.

Statistical analysis

The data were analyzed in GraphPad software. For comparisons between two groups, Student's t-test was used. For multiple group comparisons, two-way analysis of variance (ANOVA) was conducted, followed by Bonferroni's post hoc test. All data are expressed as the mean ± standard error of the mean (SEM), and statistical significance was defined as a p-value < 0.05.

References

1. Theparambil, S.M., Kopach, O., Braga, A. *et al.* Adenosine signalling to astrocytes coordinates brain metabolism and function. *Nature* **632**, 139–146 (2024).
2. Ling, E., Nemesh, J., Goldman, M. *et al.* A concerted neuron–astrocyte program declines in ageing and schizophrenia. *Nature* **627**, 604–611 (2024).
3. Bliss, T. et al. Synaptic plasticity in the anterior cingulate cortex in acute and chronic pain. *Nat Rev Neurosci* **17**, 485–496 (2016).
4. Yin Wang. et al. Astrocyte-neuron lactate transport in the ACC contributes to the occurrence of long-lasting inflammatory pain in male mice. *Neurosci. Lett*, **764** (2021).
5. Marty-Lombardi, S., Lu, S., Ambroziak, W. *et al.* Neuron–astrocyte metabolic coupling facilitates spinal plasticity and maintenance of inflammatory pain. *Nat Metab.* **6**, 494–513 (2024).
6. Zhuo, M. Cortical excitation and chronic pain. *Trends Neurosci.* **31**, 199–207 (2008).
7. Zhuo, M. Long-term potentiation in the anterior cingulate cortex and chronic pain. *Phil. Trans. R. Soc. B* **369**, 20130146 (2014).
8. Markussen, K. H. et al. The multifaceted roles of the brain glycogen. *J. Neurochem.* **168**(5), 728–743 (2023)
9. Alberini CM. et al. Astrocyte glycogen and lactate: New insights into learning and memory mechanisms. *Glia*. 1244-1262 (2018).
10. Díaz-García, C.M. Glycogen from spinal astrocytes dials up the pain. *Nat Metab.* **6**, 384–386 (2024).
11. Magistretti, P. J. & Allaman, I. A Cellular Perspective on Brain Energy Metabolism and Functional Imaging. *Neuron*. **86**, 883–901 (2015).
12. Iqbal Z, Liu S, Lei Z, Ramkrishnan AS, Akter M, Li Y. Astrocyte L-Lactate Signaling in the ACC Regulates Visceral Pain Aversive Memory in Rats. *Cells.* **12**(1), 26 (2022).
13. Reid, P. et al. Astrocyte neuronal metabolic coupling in the anterior cingulate cortex of mice with inflammatory pain. *Brain Behav Immun,* **125**, 212–225 (2025).
14. Pavlova, N. N., & Thompson, C. B. (2016). The emerging hallmarks of cancer metabolism. *Cell Metabolism,* **23**(1), 27–47.
15. DeBerardinis, R. J., & Chandel, N. S. (2016). Fundamentals of cancer metabolism. *Science Advances,* **2**(5), e1600200.
16. Vander Heiden, M. G., Cantley, L. C., & Thompson, C. B. Understanding the Warburg effect: the metabolic requirements of cell proliferation. *Science,* **324**(5930), 1029–1033 (2009).
17. Altman, B. J., Stine, Z. E., & Dang, C. V. (2016). From Krebs to clinic: glutamine metabolism to cancer therapy. *Nature Reviews Cancer,* **16**(10), 619–634.
18. Guo, F., Du, Y., Qu, FH. et al. Dissecting the Neural Circuitry for Pain Modulation and Chronic Pain: Insights from Optogenetics. *Neurosci. Bull.* **38**, 440–452 (2022).
19. Lee J. *et al*. Ganglioside GT1b prevents selective spinal synapse removal following peripheral nerve injury. *EMBO Rep.* (2025)
20. Lee J, Hwang H, Lee SJ. Distinct roles of GT1b and CSF-1 in microglia activation in nerve

injury-induced neuropathic pain. *Mol Pain*. **17** (2021)
21. Lim H. et al. GT1b functions as a novel endogenous agonist of toll-like receptor 2 inducing neuropathic pain. *EMBO J*. **39**(6) (2020)
22. Agathocleous, M., Love, N., Randlett, O. *et al.* Metabolic differentiation in the embryonic retina. *Nat Cell Biol* **14**, 859–864 (2012).
23. Xie, H., Song, J., Godfrey, J. *et al.* Glycogen metabolism is dispensable for tumour progression in clear cell renal cell carcinoma. *Nat Metab.* **3**, 327–336 (2021).
24. Ibrahim, M.M.H., Bheemanapally, K., Alhamami, H.N. *et al.* Effects of Intracerebroventricular Glycogen Phosphorylase Inhibitor CP-316,819 Infusion on Hypothalamic Glycogen Content and Metabolic Neuron AMPK Activity and Neurotransmitter Expression in Male Rat. *J Mol Neurosci.* **70**, 647–658 (2020).
25. W. -H. Shin, G. R. Lee, L. Heo, H. Lee, and C. Seok, Prediction of Protein Structure and Interaction by GALAXY protein modeling programs, *Bio Design*, **2**(1), 1-11 (2014).
26. J. Ko, H. Park, L. Heo, and C. Seok, GalaxyWEB server for protein structure prediction and refinement, *Nucleic Acids Res.* **40**(W1), W294-W297 (2012).
27. Song, Q., Wei, A., Xu, H. *et al*. An ACC–VTA–ACC positive- feedback loop mediates the persistence of neuropathic pain and emotional consequences. *Nat. Neurosci.* **27**, 272–285 (2024).
28. Gao SH. *et a*l. The projections from the anterior cingulate cortex to the nucleus accumbens and ventral tegmental area contribute to neuropathic pain-evoked aversion in rats. *Neurobiol Dis.* **140**, 104862 (2020).
29. Zhang et al. An RNA-sequencing transcriptome and splicing database of glia, neurons, and vascular cells of the cerebral cortex. *J Neurosci.* **34**(36), 11929-11947 (2014).
30. Boisvert MM, Erikson GA, Shokhirev MN, Allen NJ. The Aging Astrocyte Transcriptome from Multiple Regions of the Mouse Brain. *Cell Rep*. **22**(1), 269-285 (2018).
31. assoni, A., Farkhondeh, V., Itoh, Y. *et al.* The astrocyte transcriptome in EAE optic neuritis shows complement activation and reveals a sex difference in astrocytic C3 expression. *Sci Rep* **9**, 10010 (2019).
32. Yang CF. *et al*. Sexually dimorphic neurons in the ventromedial hypothalamus govern mating in both sexes and aggression in males. *Cell*. **9**;153(4):896-909 (2013).
33. Chan, K., Jang, M., Yoo, B. *et al.* Engineered AAVs for efficient noninvasive gene delivery to the central and peripheral nervous systems. *Nat Neurosci* **20**, 1172–1179 (2017).
34. Zhang, Y. *et al*. A transcriptomic analysis of neuropathic pain in the anterior cingulate cortex after nerve injury. *Bioengineered*, **13**(2), 2058–2075 (2022).
35. Li, J., Huang, K., Thakur, M. *et al.* Oncogenic TFE3 fusions drive OXPHOS and confer metabolic vulnerabilities in translocation renal cell carcinoma. *Nat Metab.* **7**, 478–492 (2025).
36. Gonzalez-Riano, C., Garcia, A. & Barbas, C. Metabolomics studies in brain tissue: a review. *J. Pharm. Biomed. Anal.* **130**, 141–168 (2016).
37. Xia, J., Wishart, D. Web-based inference of biological patterns, functions and pathways from metabolomic data using MetaboAnalyst. *Nat Protoc* **6**, 743–760 (2011).
38. Chan, E., Pasikanti, K. & Nicholson, J. Global urinary metabolic profiling procedures using gas chromatography–mass spectrometry. *Nat Protoc* **6**, 1483–1499 (2011).
39. Crook, A. A. & Powers, R. Quantitative NMR-Based Biomedical Metabolomics: current status and applications. *Molecules.* **25**, 1-33 (2020).
40. Pudełko-Malik, N., Drulis-Fajdasz, D., Pruss, Ł. *et al.* A single dose of glycogen phosphorylase inhibitor improves cognitive functions of aged mice and affects the concentrations of metabolites in the brain. *Sci Rep* **14**, 24123 (2024).
41. T. Matsui. *et al*., Astrocytic glycogen-derived lactate fuels the brain during exhaustive

exercise to maintain endurance capacity, *Proc. Natl. Acad. Sci. U.S.A.* **114** (24) 6358-6363 (2017).
42. Natsubori A, *et al*. Serotonergic neurons control cortical neuronal intracellular energy dynamics by modulating astrocyte-neuron lactate shuttle. *iScience*. **5** 26(1), 105830 (2023).
43. Tanga FY, Nutile-McMenemy N, DeLeo JA. The CNS role of Toll-like receptor 4 in innate neuroimmunity and painful neuropathy. *Proc Natl Acad Sci U.S.A*. **102**(16) 5856-61 (2005).
44. Chaplan SR, Bach FW, Pogrel JW, Chung JM, Yaksh TL. Quantitative assessment of tactile allodynia in the rat paw. *J Neurosci Methods*. **53**(1) 55-63 (1994).

Acknowledgements

This research was supported by the 2024 Seoul National University undergraduate independent research in Student-Directed Education (SDE) program and the National Research Foundation of Korea (RS-2024-00402116).

Author contributions

J.S.P. designed the research, performed most experiments, analyzed the data, and wrote the first draft of the paper. K.H.K. contributed to data interpretation and manuscript revision. H.W.J. crossed the RiboTag and GFAP-Cre mice to created astrocyte-specific RiboTag mice and assisted with the experimental procedures. S.J.L. supervised the project.

Figure 1. ACC glycogenolysis mediates neuropathic pain chronification.
a, Experimental scheme for the glycogen assay after neuropathic pain model surgery. **b**, von-Frey test of the neuropathic pain model. Saline + Sham (black, n = 4), Saline + SNT (red, n = 9) mice, measured at baseline (BL) and days 1, 3, and 7 post-surgery: ****$P < 0.0001$ (D3 SNT versus D3 Sham), ****$P < 0.0001$ (D7 SNT versus D7 Sham). **c**, Glycogen constant in ACC, comparison of contralateral and ipsilateral areas (time points: Sham, D0.5, D1, D3, D7): ****$P < 0.0001$ (D1 SNT contra versus ipsi), ***$P = 0.0006$ (D3 SNT contra versus ipsi). **d**, Experimental scheme for NMR and IHC after GPI-1 stereotaxic injection in the ACC. **e**, von-Frey test of the neuropathic pain model. Saline + Sham (grey, n = 5), Saline + SNT (black, n = 10), GPI-1 + SNT (red, n = 10), GPI-2 + SNT (orange, n = 10) mice, measured at baseline (BL) and days 1, 3, 5, and 7 post-surgery: **$P = 0.0035$ (D3 GPI-1 + SNT versus Saline + SNT), **$P = 0.0018$ (D3 GPI-2 + SNT versus Saline + SNT), ****$P < 0.0001$ (D5, D7 GPI-1 + SNT, GPI-2 + SNT versus Saline + SNT). **f**, NMR analysis of the G1P constant in contraACC areas. Saline + SNT: n = 4, Saline + Sham: n = 3, GPI-1 + SNT: n = 4, GPI-2 + SNT: n = 4: **$P = 0.0020$ (GPI-1 + SNT versus Saline + SNT), ***$P = 0.0010$ GPI-2 + SNT versus Saline + SNT). **g**, Representative confocal images of the ACC (scale bar, 200 μm). **h**, IHC data for c-Fos+/NeuN+ cells in the ACC. (Left): Number of c-Fos+/NeuN+ cells in contraACC areas: **$P = 0.0062$ (Saline + Sham versus Saline + SNT), ****$P < 0.0001$ (GPI-1 + SNT and GPI-2 + SNT versus Saline + SNT). (Right): Ratio of c-Fos+/NeuN+ cells in contraACC areas, compared with ipsiACC areas: **$P = 0.0029$ (Saline + Sham versus Saline + SNT), ****$P < 0.0001$ (GPI-1 + SNT and GPI-2 + SNT versus Saline + SNT). Data are represented as the mean ± SEM; two-way ANOVA and t-test.

Figure 2. Astrocyte-specific mechanism underlies altered glycogen dynamics and pain chronification.

a, Scheme of the glycogen metabolism pathway (created with https://www.biorender.com). **b**, Glycogen metabolism genes (*Ppp1r3c, Gys1, Phka2, Pygb*) and single-cell RNA-sequencing expression results for each cell type. **c**, Schematic illustration of $GFAP^{Cre}$::RiboTag mice and the neuropathic pain model transcriptomics experiment. **d**, qPCR data for glycogen metabolism genes (*Ppp1r3c, Gys1, Phka2, Pygb*), expressed as fold changes (time points: days 1, 3, and 7; n = 6). **e**, Experimental scheme for IHC after AAV-Caspase3 virus injection and SNT surgery. **f**, Representative confocal images of ACCs with anti-s100β staining. **g**, von-Frey test of the neuropathic pain model. tdTomato + Sham (grey, n = 5), tdTomato + SNT (black, n = 8), Casp3 + SNT (blue, n = 12) mice, measured at baseline (BL) and days 1, 3, 5, 7, 10, and 14 post-surgery: ***$P = 0.0010$ (D5 Casp3 + SNT versus tdTomato + SNT), ****$P < 0.0001$ (D7, D10 and D14 Casp3 + SNT versus tdTomato + SNT). **h**, Representative confocal images of ACCs (scale bar, 200 μm). **i–j**, IHC data for c-Fos+/NeuN+ cells in ACCs. **i**, tdTomato and Casp3 injection group analyses. (Left): Number of c-Fos+/NeuN+ cells in contraACC areas: ****$P < 0.0001$ (tdTomato + Sham and Casp3 + SNT versus tdTomato + SNT). (Right): Ratio of c-Fos+/NeuN+ cells in contraACC areas compared with ipsiACC areas: *$P = 0.0062$ (tdTomato + Sham versus tdTomato + SNT), ****$P < 0.0001$ (Casp3 + SNT versus tdTomato + SNT). **j**, Comparison between IHC data and the GPI injection experiment. (Left): Number of c-Fos+/NeuN+ cells in contraACC areas (no significant differences). (Right): Ratio of c-Fos+/NeuN+ cells in contraACC areas compared with ipsiACC areas (no significant differences). Data are represented as the mean ± SEM; two-way ANOVA-multiple comparisons and t-test.

Figure 3. Identification of ACC metabolic dynamics during neuropathic pain chronification.

a, Schematic illustration of GFAP^{Cre}::RiboTag mice and the neuropathic pain model transcriptomics experiment. **b**, qPCR data for Warburg effect genes (*Hif-1a, Ldha, Ldhb, Mct4;* n = 6), expressed as fold changes (time points: day 1, 3, and 7, each time point: n = 6). **c**, Experimental scheme for the GC-MS metabolomics analysis of the SNT pain model. **d**, Heatmap of metabolite fold changes relative to the sham condition at 12 h and days 1, 3, and 7 (n = 3 per time point). The data are $\log_2$-transformed and Z-score normalized. **e–f**, Pathway enrichment analyses of GC-MS metabolomics data. Selected high-enrichment metabolic pathways are labeled. **e**, 12 h after SNT. **f**, 7 days after SNT. **g**, Analysis of the time-dependent enrichment of selected cancer-associated pathways (time points: 12 h and 1, 3, and 7 days). Data are represented as the mean ± SEM. The pathway enrichment analysis of GC-MS data was performed using MetaboAnalyst v6.0. (http://www.metaboanalyst.ca).

Figure 4. ACC glycogenolysis mediates cancer-associated metabolic changes during neuropathic pain chronification.

a, Experimental scheme for the NMR metabolomics analysis of the SNT pain model. **b–k**, Metabolite concentration data from the NMR analysis. Saline + SNT: n = 4, Saline + Sham: n = 3, GPI-1 + SNT: n = 4, GPI-2 + SNT: n = 4. **b**, Lactate concentration in each group: $^{**}P = 0.0084$ (Saline + Sham versus Saline + SNT), $^{*}P = 0.0141$ (GPI-1 + SNT versus Saline + SNT), $^{**}P = 0.0010$ (GPI-2 + SNT versus Saline + SNT). **c**, Pyruvate concentration in each group: $^{****}P < 0.0001$ (Saline + Sham versus Saline + SNT), $^{****}P < 0.0001$ (GPI-2 + SNT versus Saline + SNT). **d**, Succinate concentration in each group: $^{****}P < 0.0001$ (Saline + Sham versus Saline + SNT), $^{**}P = 0.0046$ (GPI-1 + SNT versus Saline + SNT), $^{**}P = 0.0010$ (GPI-2 + SNT versus Saline + SNT). **e**, Malate concentration in each group: $^{**}P = 0.0065$ (GPI-1 + SNT versus Saline + SNT), $^{***}P = 0.0001$ (GPI-2 + SNT versus Saline + SNT). **f**, Glutamate concentration in each group: $^{**}P = 0.0056$ (Saline + Sham versus Saline + SNT), $^{****}P < 0.0001$ (GPI-2 + SNT versus Saline + SNT). **g**, Glutamine concentration in each group: $^{*}P = 0.0240$ (GPI-2 + SNT versus Saline + SNT). **h**, GABA concentration in each group (no significant differences). **i**, Alanine concentration in each group: $^{*}P = 0.0443$ (Saline + Sham versus Saline + SNT), $^{**}P = 0.0044$ (GPI-2 + SNT versus Saline + SNT). **j**, Arginine concentration in each group: $^{***}P = 0.0009$ (Saline + Sham versus Saline + SNT). **k**, Taurine concentration in each group: $^{*}P = 0.0282$ (Saline + Sham versus Saline + SNT), $^{**}P = 0.0024$ (GPI-2 + SNT versus Saline + SNT). **l**, Scheme for selected metabolic pathways. **m–n**, Pathway enrichment analysis comparing the **m**, Warburg effect pathway and **n**, glutamate metabolism pathway. Data are represented as the mean ± SEM; t-test. The pathway enrichment analysis of NMR data was performed using MetaboAnalyst v6.0. (http://www.metaboanalyst.ca).

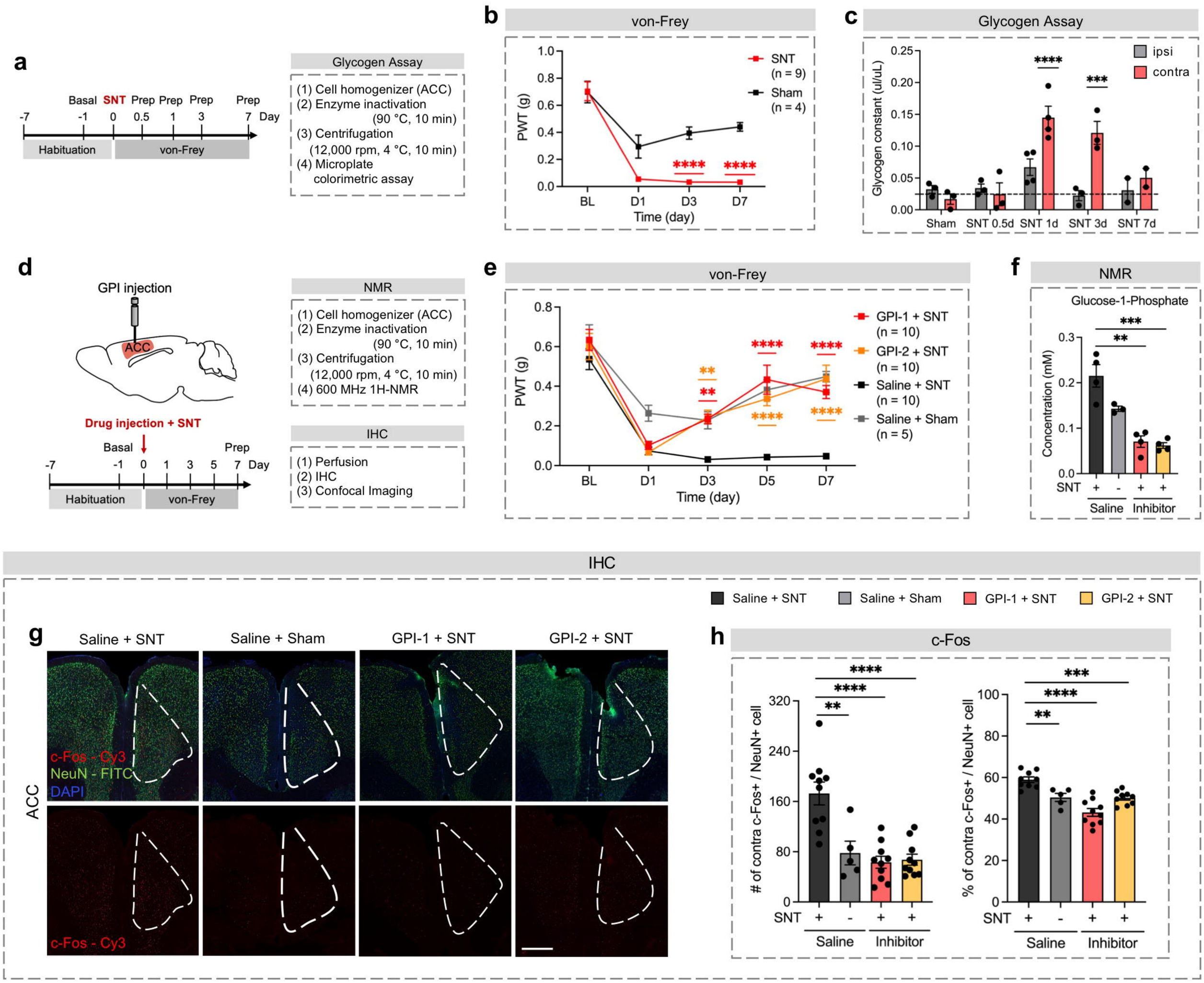

Figure 1. ACC glycogenolysis mediates neuropathic pain chronification.

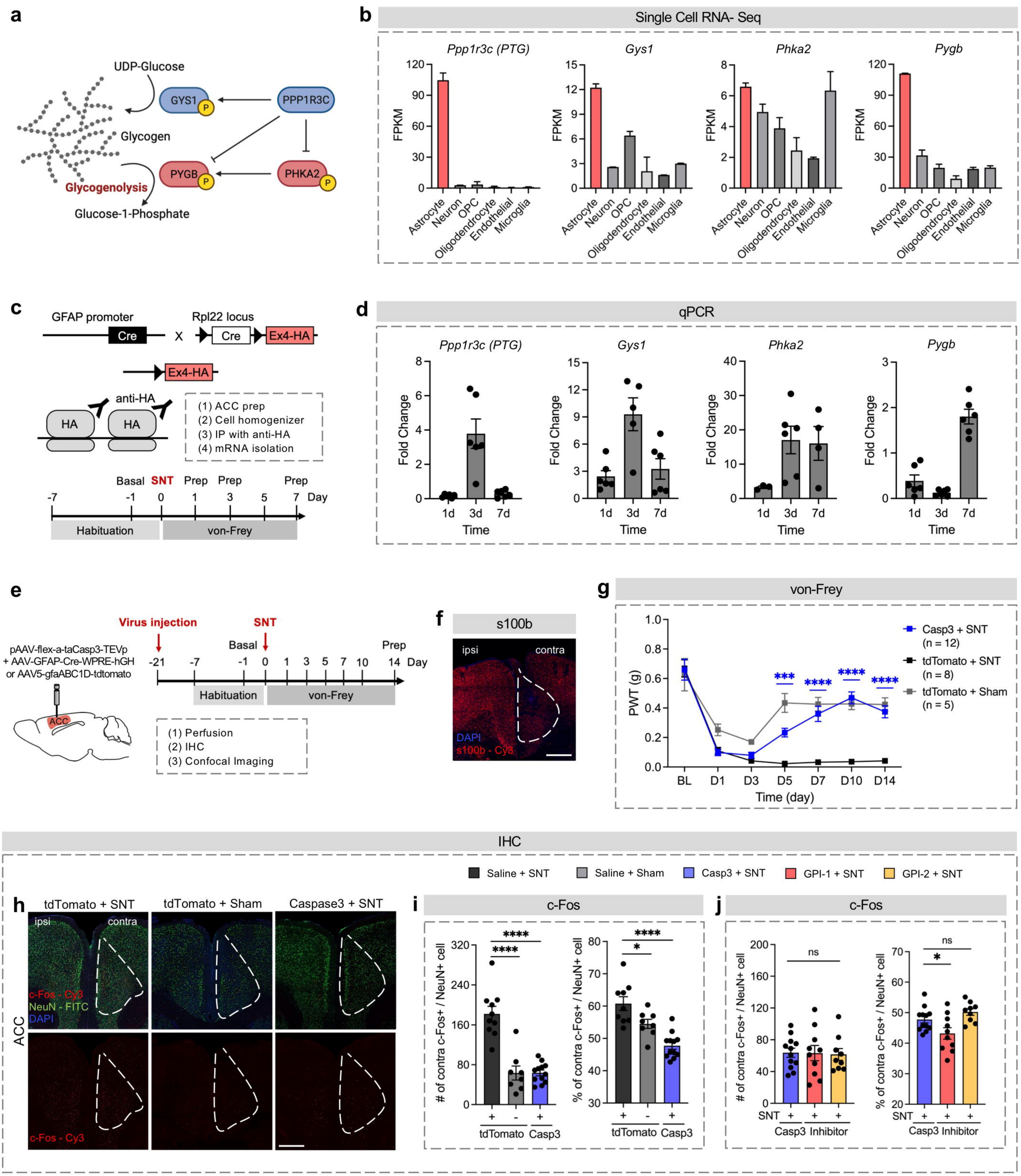

Figure 2. Astrocyte-specific mechanisms underlie altered glycogen dynamics and pain chronification.

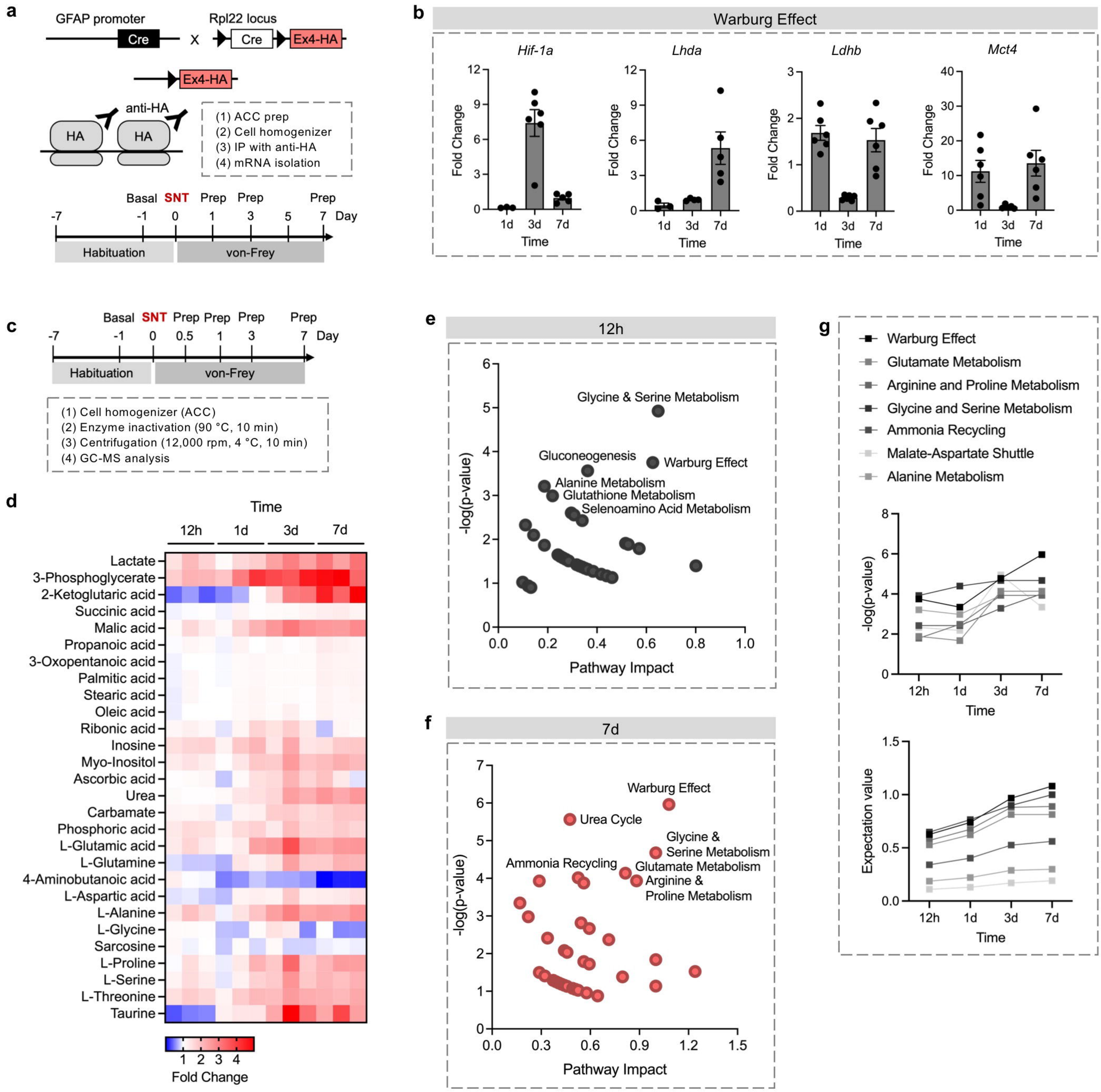

Figure 3. Identification of ACC metabolic dynamics during neuropathic pain chronification.

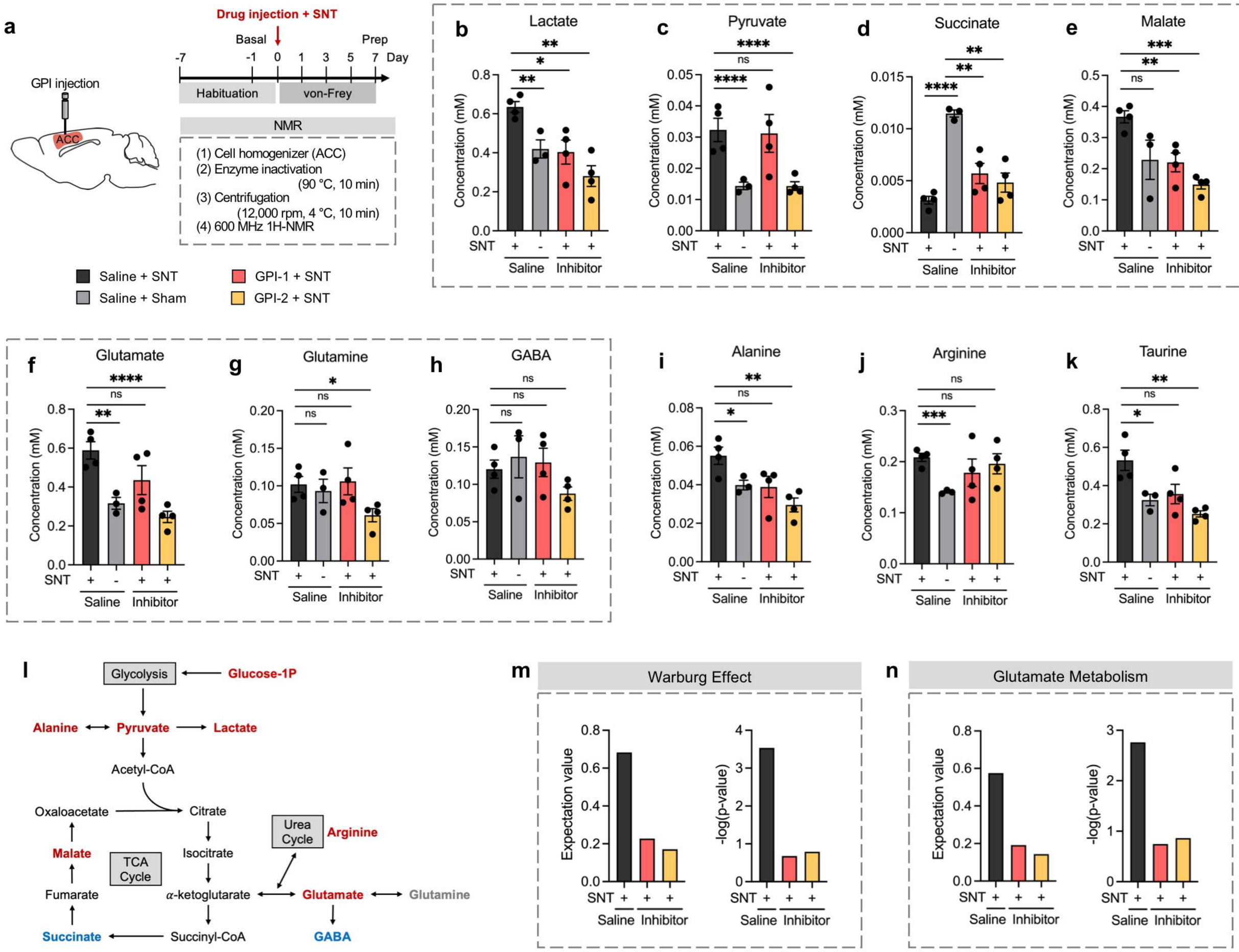

Figure 4. ACC glycogenolysis mediates cancer-associated metabolic changes in neuropathic pain chronification.